

Modeling two-phase flow in PEM fuel cell channels

Yun Wang¹, Suman Basu, Chao-Yang Wang*

*Electrochemical Engine Center (ECEC), and Department of Mechanical and Nuclear Engineering,
The Pennsylvania State University, University Park, PA 16802, USA*

Received 19 December 2007; received in revised form 23 January 2008; accepted 24 January 2008

Available online 3 February 2008

Abstract

This paper is concerned with the simultaneous flow of liquid water and gaseous reactants in mini-channels of a proton exchange membrane (PEM) fuel cell. Envisaging the mini-channels as structured and ordered porous media, we develop a continuum model of two-phase channel flow based on two-phase Darcy's law and the M^2 formalism, which allow estimate of the parameters key to fuel cell operation such as overall pressure drop and liquid saturation profiles along the axial flow direction. Analytical solutions of liquid water saturation and species concentrations along the channel are derived to explore the dependences of these physical variables vital to cell performance on operating parameters such as flow stoichiometric ratio and relative humidity. The two-phase channel model is further implemented for three-dimensional numerical simulations of two-phase, multi-component transport in a single fuel-cell channel. Three issues critical to optimizing channel design and mitigating channel flooding in PEM fuel cells are fully discussed: liquid water buildup towards the fuel cell outlet, saturation spike in the vicinity of flow cross-sectional heterogeneity, and two-phase pressure drop. Both the two-phase model and analytical solutions presented in this paper may be applicable to more general two-phase flow phenomena through mini- and micro-channels.

© 2008 Elsevier B.V. All rights reserved.

Keywords: Mathematical modeling; Proton exchange membrane fuel cells; Water management; Two-phase flow; Channel flow

1. Introduction

Fuel cells, converting chemical energy of fuels directly into electricity, have become an integral part of alternative energy and energy efficiency. Their noteworthy features, high-energy conversion efficiency and zero emission, meet the critical demands of a rapidly growing society [1,2]. Among all types of fuel cells, the proton exchange membrane (PEM) fuel cell, also called polymer electrolyte fuel cell (PEFC), has reached center stage, particularly for mobile and portable applications [3,4]. Besides their high-power capability, PEM fuel cells work at low temperatures, produce only water as byproduct, and can be compactly assembled, making them one of the leading candidates for the next generation power generator.

A typical PEFC consists of bipolar plates, gas channels, gas diffusion layers (GDLs), and a proton-conductive membrane

with platinum catalyst coated on each side, called the membrane electrode assembly (MEA), as shown in Fig. 1. Gas channels are grooved in graphite or metal plates, where injected reactant streams are distributed for electrochemical reactions. The GDLs, usually coated with micro-porous layers (MPLs), play an important role in electronic connection between the bipolar plate and the electrode and provide a passage for reactant transport and heat/water removal. Protons are produced from hydrogen oxidation in the anode catalyst layer, and pass through the membrane, carrying water molecules via electro-osmotic drag, to the cathode catalyst layer where the oxygen reduction reaction (ORR) occurs with water as byproduct.

Water management is a central issue in PEFC technology because while water is essential for membrane ionic conductivity, excess liquid water leads to flooding of catalyst layers and GDLs [5–7] as well as channel clogging [8,9]. Given low-operating temperatures during normal startup (25 °C) and hence low-saturation pressures, two-phase phenomena are unavoidable in automotive fuel cells. Two-phase transport in a fuel cell consists of three sub-problems: catalyst layer flooding, GDL flooding, and two-phase flow in channels. To date, most of the efforts in two-phase modeling were devoted to the former two

* Corresponding author. Tel.: +1 814 863 4762; fax: +1 814 863 4848.

E-mail address: cwx31@psu.edu (C.-Y. Wang).

¹ Present address: Department of Mechanical and Aerospace Engineering, University of California, Irvine, CA 92697-3975, USA.

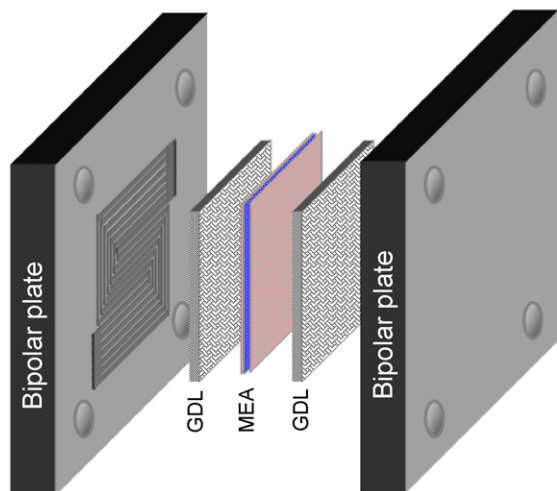


Fig. 1. Schematic of a PEM fuel cell.

[5,10–18], and few models for channel flooding have existed in the literature.

In practice, however, two-phase flow and transport in channels is of paramount importance for fuel cell operation, particularly in the most energy-efficient regime involving high-cell voltage and therefore low-current density. In this regime, flow rates of hydrogen and air through channels are exceedingly low, resulting in substantial liquid water accumulation. Fig. 2 shows experimental data of cell voltage and cathode-side pressure drop as functions of air stoichiometry. It can be seen that channel flooding at low stoichiometry ($\xi = 2$) results in cell voltage drop of as much as 120 mV, which would negate a voltage gain of 45 mV targeted by fourfold improvement in catalyst activity. Moreover, the drastic fluctuation in cell voltage at low stoichiometry sets up voltage cycling at high potentials, which has severe impact on PEM fuel cell durability. Other major concerns of channel flooding include: (1) fuel starvation which leads to carbon corrosion in the cathode catalyst layer; (2) oxygen starvation which leads to hydrogen evolution on the cathode and furthermore H_2/O_2 combustion and hot spot formation; (3) flow maldistribution among parallel channels, leading to operational

instability and efficiency losses; (4) increase of the mass transport loss at high-current densities. Thus, an urgent need in PEFC modeling has been to develop a two-phase flow and flooding model for fuel cell channels, allowing the liquid water saturation to be predicted at levels as high as 15–20%. Developing such a preliminary model is the objective of this work.

In this work, we envision a structural and flow analogy between PEM fuel cell channels and random porous media. Following the analogy, we then apply two-phase flow theory in porous media to describe the two-phase, multi-component transport in channels of a fuel cell. We show that such a phenomenological model is able to capture pressure, liquid saturation and reactant composition distributions along the flow, thereby sufficing to address such questions as channel flooding, water trapping in channels of heterogeneous geometry, two-phase flow maldistribution in multiple, parallel channels, and the flowfield effect on liquid water drainage. In addition, we present analytical solutions as to the saturation distribution along the channel and analysis on the heterogeneity impact and two-phase pressure factor for PEFC channels for the first time as well as three-dimensional numerical simulations to explore the effects of key parameters such as relative humidity (RH) and air stoichiometric ratio on two-phase flow in channels. Finally, experimental validation of the predicted two-phase pressure drop is reported.

2. Analogy between mini-channels and random porous media

PEM fuel cell channels are characterized by parallel or serpentine channels with square, rectangular or trapezoid cross-sections and channel dimensions ranging from 0.1 to 1 mm (see Figs. 3 and 4) [2,19]. Different configurations have been described and explored recently, such as serpentine, parallel, and interdigitated flow fields [19–23]. Fig. 4 shows a typical serpentine parallel flow field in an industrial PEFC [24]. Visualization studies have revealed and studied two-phase phenomena in fuel cell channels experimentally [8,9,25], as illustrated in Fig. 5. Channels of similar structure are also encountered in

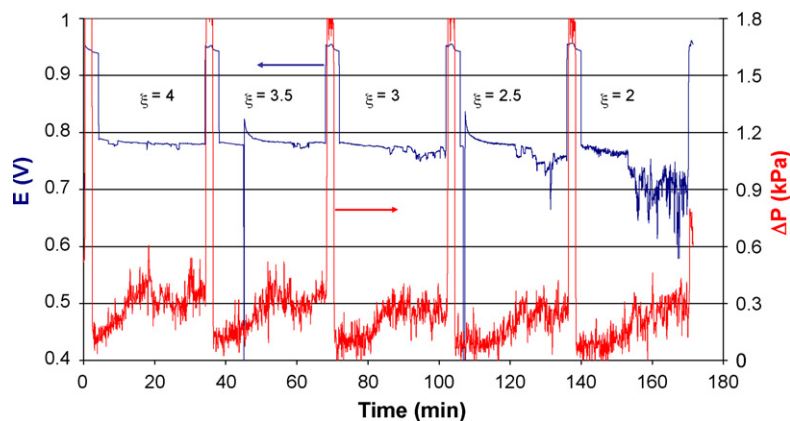


Fig. 2. Cell voltage and cathode-side pressure drop measured under various air stoichiometric ratios (symbolized by ξ in the figure) in a 14 cm^2 fuel cell for 0.2 A cm^{-2} , 150 kPa and 80°C with the dew point of both H_2 and air at 70°C [54]. As the air stoichiometry decreases, the pressure drop does not decrease proportionally, indicating the onset of severe water flooding in cathode channels. Simultaneously, the cell voltage drops by as much as 120 mV and fluctuates more.

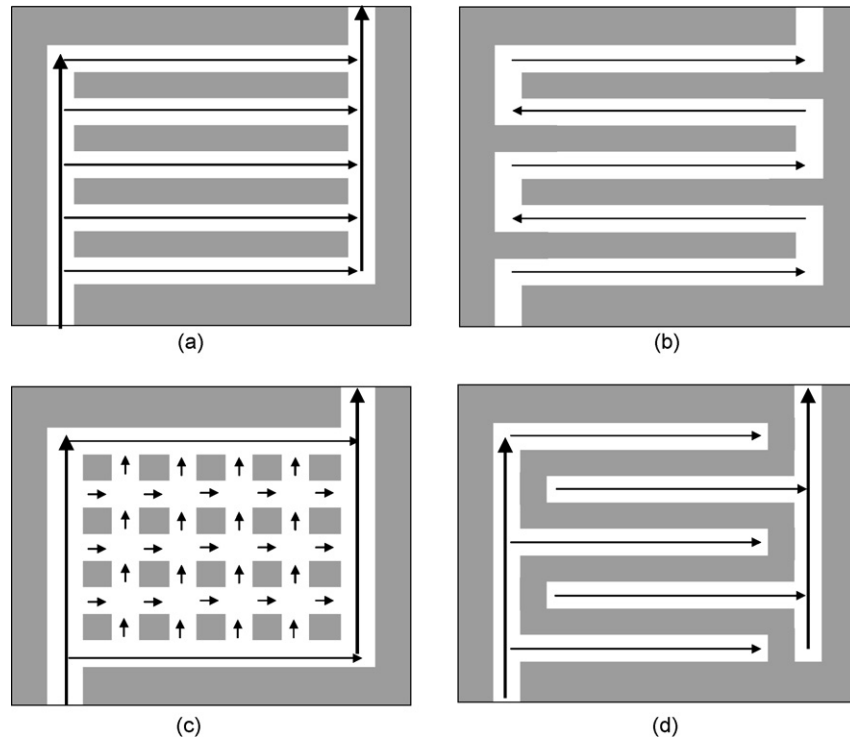


Fig. 3. Typical flow fields of PEFCs. (a) Parallel flow field; (b) serpentine flow field; (c) pin flow field; (d) interdigitated flow field.

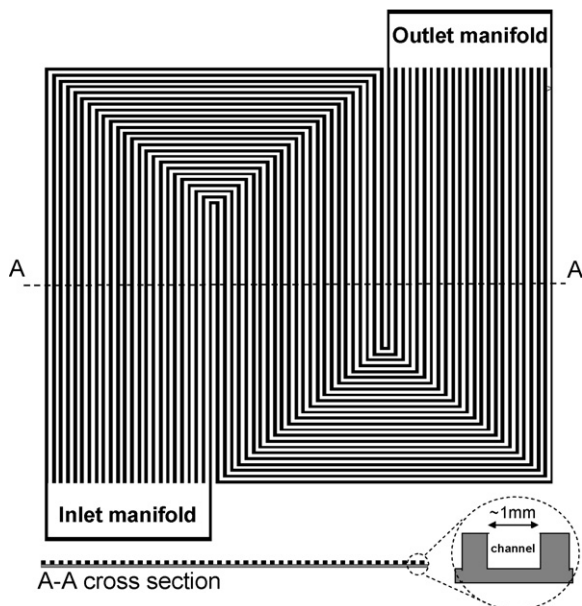


Fig. 4. A flow field of an industrial PEFC [24].

miniature heat pipes and micro-heat exchangers. In these applications, evaporation and condensation take place to utilize the efficient latent heat transfer, therefore two-phase flow is ubiquitous. Previous studies in these fields include those of Stubos et al. [26], Wang et al. [27], Tio et al. [28], Imke [29], Henning et al. [30], and Sugumar and Tio [31].

Another field worthy mentioning is two-phase flow in geological media or petroleum reservoirs. Flow beds in these applications feature random solid particles with two-phase flow in pores. Some porous formations feature a pore size range of ~ 1 mm, thus strongly resembling the fuel cell channels. The structural similarity between the two, with the former being random porous media and the latter regular, ordered pores, was recognized by Chaouche et al. [32], Or and Tuller [33], and Li et al. [34]. In addition, there exists a flow analogy in that flow in fuel cell channels is well within the laminar regime and exhibits a linear relationship between the pressure drop and velocity, the same relation as expressed by Darcy’s law for flow in porous media. Indeed, the proportionality constant called hydraulic conductance in laminar flow through channels is physically equivalent to permeability of a porous medium. Such a flow analogy was recognized by Chen [35], Wong et al. [36], Wang et al. [27], and

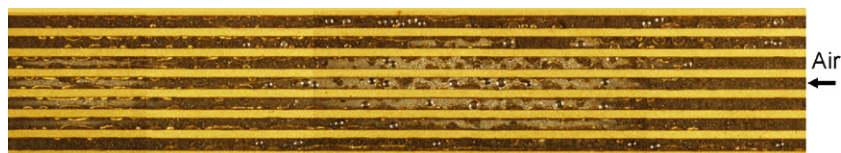


Fig. 5. Visualization of two-phase flow in PEM fuel cell channels [55].

Tio et al. [28], among others. In addition, the geometrical analogy between a porous medium and a capillary is traditionally employed to understand and develop flow theories in irregular porous media, in which disordered porous media with tortuous pore channels are simplified as a bundle of straight capillary tubes. Envisaging the geometrical and flow analogy between fuel cell channels and random porous media, we seek to develop a macroscopic model for two-phase flow in fuel cell channels by using the two-phase Darcy's flow theory, as detailed in the next section. Similar approaches were successfully implemented by Wang et al. [27], Tio et al. [28], and Imke [29] for miniature heat pipes and micro-heat exchangers.

3. Physical model

Fig. 1 schematically shows the geometry of a PEFC and its components. The focus is placed on a single straight channel in order to develop a channel two-phase flow model resolving axial variations in pressure, liquid saturation and other quantities. This is schematically shown in Fig. 6(a) for the cathode side. Partially or fully humidified air is fed in the inlet, and liquid water produced from ORR is injected into the channel from the sidewall facing the GDL. The channels can generally be treated as porous media with or without porous inserts. Without porous inserts, the pore size in the porous medium is exactly equal to the channel cross-section dimension with the pore tortuosity and porosity equal to unity. This general porous approach is illustrated in Fig. 6(b) and the Darcy's law is applied to describe the two-phase flow through the channels, provided that the Reynolds number based on the pore size is much smaller than 2000 to ensure laminar flow. This condition is commonly met in fuel cell operation. Also, the capillary number denoting the ratio of viscous force to surface tension is unimportant for channel two-phase flow in the presence of large axial velocity in gas channels.

3.1. Conservation of mass and momentum

In the channel pores, we consider the gas and liquid phases as constituents of a two-phase mixture with distinct phase velocities. Following the well-known multiphase mixture formulation

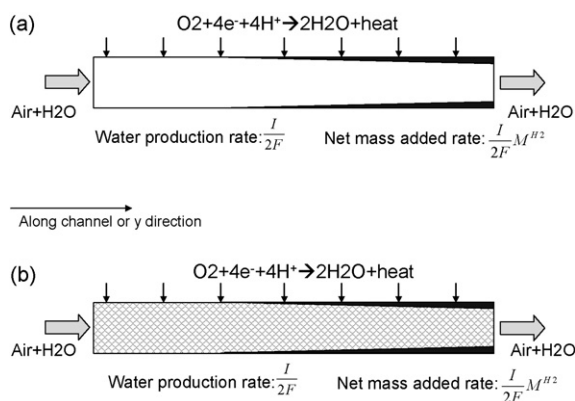


Fig. 6. Schematic of two-phase flow through a single channel: (a) an open channel; (b) a channel with porous inserts. The black shadowed regions on the upper or lower wall represent the liquid phase.

for two-phase flow through porous media [37], the mass and momentum conservations of the two-phase mixture can be written as follows:

$$\text{Continuity equation: } \varepsilon \frac{\partial \rho}{\partial t} + \nabla \cdot (\rho \vec{u}) = 0 \quad (1)$$

$$\text{Momentum conservation: } \rho \vec{u} = -\frac{K}{\nu} (\nabla P - \gamma_\rho \rho \vec{g}) \quad (2)$$

where the physical properties of the two-phase mixture are defined as

$$\rho = s\rho_l + (1-s)\rho_g \quad (3)$$

$$\rho \vec{u} = \vec{u}_l \rho_l + \vec{u}_g \rho_g \quad (4)$$

$$\nu = \left(\frac{k_{rl}}{v_l} + \frac{k_{rg}}{v_g} \right)^{-1} \quad (5)$$

Here, the liquid water saturation, s , is defined as the volume fraction of open pores occupied by liquid water, which is a key parameter characterizing the two-phase flow. Liquid saturation is identical to liquid volume fraction in channel two-phase flow. The liquid saturation can be determined from the following relation with the mixture water concentration, C^{H_2O} , after the latter is solved from the water transport equation:

$$s = \frac{C^{H_2O} - C_{sat}}{\rho_l / M^{H_2O} - C_{sat}} \quad (6)$$

The density correction factor in Eq. (2), γ_ρ , is a sole function of phase saturations and thus can be regarded as a property of the two-phase mixture:

$$\gamma_\rho = \frac{\rho_l \lambda_l + \rho_g \lambda_g}{s\rho_l + (1-s)\rho_g} \quad (7)$$

where the phase mobility, λ_k , is defined as

$$\lambda_l = \frac{k_{rl}/v_l}{k_{rl}/v_l + k_{rg}/v_g}, \quad \text{and} \quad \lambda_g = 1 - \lambda_l \quad (8)$$

The relationship between the phase mobility, λ_k , and liquid water saturation, s , is plotted in Fig. 7. It can be seen that the

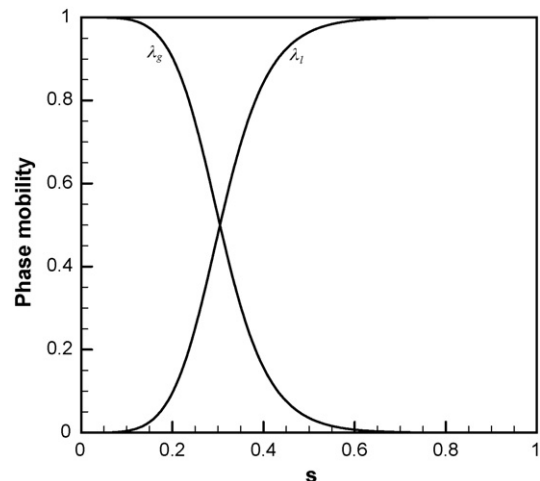


Fig. 7. Phase mobility vs. liquid water saturation ($n_k = 4$).

liquid mobility increases with liquid saturation. The relative permeability, k_{rk} , is defined as the ratio of the intrinsic permeability of liquid/gas phase to the total permeability of a porous medium. Physically, it describes the extent to which one fluid is hindered by others in pore spaces and hence can be formulated as a function of liquid saturation. A common set of functions have been used in the literature:

$$k_{rl} = \left(\frac{s - s_{ir}}{1 - s_{ir}} \right)^{n_k} \quad \text{and} \quad k_{rg} = \left(1 - \frac{s - s_{ir}}{1 - s_{ir}} \right)^{n_k} \quad (9)$$

Berning and Djilali [38] set n_k equal to unity in their work, a linear relationship also called X curve, while some used the value of 3 or 4 [6,13,16,17]. Note that the larger n_k is, the greater the degree to which the liquid water affects the gas flow. In the present work, we use $n_k = 4$ following Corey [39].

The irreducible residual saturation, s_{ir} , is physically the liquid fraction bound inside the capillary channel by surface tension force and hence cannot be removed by drainage but only by evaporation. The value of s_{ir} is determined by the balance between surface tension force, σ , and gravitational force, and is suggested by Saez and Carbonell [40] for mini-channels in the follow function of Eotvos number, $E\ddot{o}$:

$$s_{ir} = \frac{1}{20 + 0.9E\ddot{o}} \quad (10)$$

The Eotvos number is defined by:

$$E\ddot{o} = \frac{\rho_l g d_h^2}{\sigma} \quad (11)$$

where d_h is the hydraulic diameter of the channel.

Once k_{rk} is available, the following Darcy’s law is applied to calculate the velocity for each phase:

$$\rho_k \vec{u}_k = -k_{rk} \frac{K}{\nu_k} (\nabla P_k - \rho_k \vec{g}) \quad (12)$$

In addition, a dimensionless number, Bo, is defined as the ratio of the gravitational force to the surface tension, $Bo = (g \Delta\rho/\sigma)d_h^2$ where $\Delta\rho$, d_h and σ are the density difference between phases, the channel hydraulic diameter and surface tension, respectively. Bo is typically small in fuel cells (<0.1); therefore, the gravitational term in Eq. (12) can be neglected.

Cathode gas channels commonly feature a constant flow as Wang and Wang demonstrated that the flow variations due to ORR and phase change is less than 4% [45]. Under this assumption, the porous medium permeability, K , can be determined from the hydraulic conductance of laminar flow through a flow channel of various cross-sections. It is usually obtained, under single-phase condition, through the well-known Hagen–Poiseuille equation:

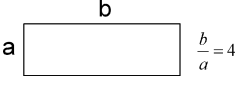
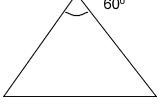
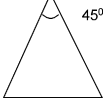
$$K = c \frac{d_h^2}{32} \quad (13)$$

where the hydraulic diameter of the channel is given by

$$d_h = 4 \times \frac{\text{cross-section area}}{\text{channel perimeter}} \quad (14)$$

Table 1

Flow shape factors for typical channel cross-sections in PEM fuel cells [27]

Shape	c
	1.0
	1.127
	0.874
	1.2
	1.202

and c is a factor determined by the cross-section shape, which is also called flow shape factor. For convenience, some c values have been listed in Table 1 for several typical cross-sections of fuel cell channels.

3.2. Conservation of species

The primary species in PEFC channels include hydrogen, water, and nitrogen in the anode, and oxygen, nitrogen, and water in the cathode side. A general form of species transport equation for both single- and two-phase mixtures can be expressed by [37]:

$$\begin{aligned} \text{Species conservation :} \quad & \varepsilon \frac{\partial C^k}{\partial t} + \nabla \cdot (\gamma_c \vec{u} C^k) \\ & = \nabla \cdot (D_g^{k,\text{eff}} \nabla C_g^k) - \nabla \cdot \left[\left(\frac{m f_1^k}{M^k} - \frac{C_g^k}{\rho_g} \right) \vec{j}_1 \right] \end{aligned} \quad (15)$$

where γ_c is called the convection correction factor to correct the convective transport of the two-phase mixture due to difference between phase velocities. Assuming that other species, such as oxygen, hydrogen, and nitrogen, have a negligible solubility in the liquid water, γ_c can be expressed as

$$\gamma_c = \begin{cases} \frac{\rho}{C_{\text{H}_2\text{O}}} \left(\frac{\lambda_1}{M_{\text{H}_2\text{O}}} + \frac{\lambda_g}{\rho_g} C_{\text{sat}}^{\text{H}_2\text{O}} \right), & \text{for water} \\ \frac{\rho \lambda_g}{\rho_g (1 - s)}, & \text{for other species} \end{cases} \quad (16)$$

In Eq. (15), the first term on the right side describes the effect of the molecular diffusive transport. As more than two species are present in a fuel cell, the multi-component Stefan–Maxwell diffusion is usually applied. To simplify the model expression

and later numerical implementation, we use the Fick's law to describe the molecular diffusion in the gaseous phase. In addition, Eq. (15) also neglects diffusion of hydrogen, oxygen, and nitrogen in liquid water due to exceedingly low solubility. In the gas phase, the species diffusion coefficient in Eq. (15) is given by [41]:

$$D_g^k = D_{g,o}^k \left(\frac{T}{353} \right)^{3/2} \left(\frac{1}{p} \right) \quad (17)$$

In a two-phase region, the effective gaseous diffusion coefficient is modified via the Bruggeman correlation:

$$D_g^{k,\text{eff}} = (1-s)^{\tau_d} D_g^k \quad (18)$$

In addition to the convective and diffusive transport, capillary action may take place in porous media, which drives liquid water from a higher liquid saturation region to a lower one. The water flux driven by the capillary force is called the capillary diffusion flux, \vec{j}_l , which is included in the second term of Eq. (15). The capillary force is mathematically described by capillary pressure, p_c , which is defined as the pressure difference between gas and liquid phases, i.e. $p_g - p_l$. The capillary pressure is a function of surface properties such as surface tension, σ , and contact angle, θ_c , porous medium properties such as porosity, ε , and permeability, K , and the liquid saturation, s . The capillary diffusion flux, \vec{j}_l , and capillary pressure, p_c , can be calculated by

$$\vec{j}_l = \frac{\lambda_l \lambda_g}{\nu} K [\nabla p_c + (\rho_l - \rho_g) \vec{g}] \quad (19)$$

where

$$p_c = \sigma \cos(\theta_c) \left(\frac{\varepsilon}{K} \right)^{1/2} J(s)$$

Here, $J(s)$ is the Leverett function, an empirical relation that is generally adopted for both hydrophobic and hydrophilic porous media [7], and we extend it to structured porous medium representation of gas channels:

$$J(s) = \begin{cases} 1.417(1-s) - 2.120(1-s)^2 + 1.263(1-s)^3, & \text{for } \theta_c < 90^\circ \\ 1.417s - 2.120s^2 + 1.263s^3, & \text{for } \theta_c > 90^\circ \end{cases} \quad (20)$$

Usually, the GDL materials are made hydrophobic through adding PTFE to facilitate the water removal from the channel–GDL interface [42]. Other channel walls are usually hydrophilic, allowing wicking of liquid water away from the GDL surface.

3.3. Conservation of energy

Temperature distribution plays a vital role in channel two-phase flow due to the exponential relationship between the saturation pressure, p_{sat} , and temperature. Springer et al. [43] correlated p_{sat} with temperature:

$$\log_{10} p_{\text{sat}} = -2.1794 + 0.02953(T - 273.15) - 9.1837 \times 10^{-5}(T - 273.15)^2 + 1.4454 \times 10^{-7}(T - 273.15)^3 \quad (21)$$

A general thermal model for two-phase flow can be written as

$$\begin{aligned} \text{Energy conservation : } & \frac{\partial \rho c_p T}{\partial t} + \nabla \cdot (\gamma_T \rho c_p \vec{u} T) \\ & = \nabla \cdot (k^{\text{eff}} \nabla T) + S_{\text{fg}} \end{aligned} \quad (22)$$

Once again, the advection term is modified by a correction factor, γ_T , and is given by

$$\gamma_T = \frac{\rho(\lambda_l c_{p,l} + \lambda_g c_{p,g})}{s \rho_l c_{p,l} + (1-s) \rho_g c_{p,g}} \quad (23)$$

The source term arises from latent heat release or absorption due to water condensation/evaporation and can be written as [16]

$$S_{\text{fg}} = h_{\text{fg}} \dot{m}_{\text{fg}} \quad (24)$$

where h_{fg} and \dot{m}_{fg} are the latent heat of vapor–liquid phase change and the phase change rate, respectively. The latter is readily calculated from the liquid continuity equation, namely

$$\dot{m}_{\text{fg}} = \rho_l \frac{\partial s}{\partial t} + \nabla \cdot (\rho_l \vec{u}_l) \quad (25)$$

where the liquid-phase velocity in the M^2 model is computed from either Eq. (12) or the following equation:

$$\rho_l \vec{u}_l = \vec{j}_l + \lambda_l \rho \vec{u} \quad (26)$$

3.4. Boundary conditions

Eqs. (1), (2), (15) and (22) form a complete set of governing equations with unknowns of \vec{u} , P , T , and C^k to describe non-isothermal, two-phase flow in fuel cell channels. Proper boundary conditions are needed to close the mathematical system. The temperature distribution is usually determined by the

cooling channel design in PEFCs, as detailed previously by Wang and Wang [24]. Other boundary conditions are specified as follows.

3.4.1. Flow inlet boundaries

The cathode inlet flow is commonly set partially or fully saturated without liquid water. Therefore, the inlet mixture velocity is the one in the gas phase, $\vec{u}_{\text{in,g}}$, determined by the stoichiometric flow ratio, ξ_c , and a reference/average current density, I_{av} :

$$\xi_c = \frac{C^{\text{O}_2} u_{\text{in,g}} A_{xz}}{I_{\text{av}} A_{\text{mem}} / 4F} \quad (27)$$

where A_{xz} and A_{mem} are the areas of flow cross-sectional and the membrane, respectively. The inlet molar concentrations are determined by the inlet pressure and humidity according to the ideal gas law.

3.4.2. Outlet boundaries

Fully developed conditions are applied:

$$\frac{\partial \vec{u}}{\partial n} = 0 \quad \text{and} \quad \frac{\partial C^k}{\partial n} = 0 \quad (28)$$

3.4.3. Solid wall

Slip and impermeable velocity condition and no-flux condition are applied:

$$\vec{u} \cdot \vec{n} = 0 \quad \text{and} \quad \frac{\partial C^k}{\partial n} = 0 \quad (29)$$

3.4.4. GDL surface

As only the flow channel is considered, during operation product water is injected into the channel at the GDL–channel interface and simultaneously a proportional amount of oxygen is transported out of channel for the ORR in the catalyst layer. Given a distribution of current density, $I(x,y)$, one can calculate the water production and oxygen consumption rates via the Faraday's law:

$$S_{\text{H}_2\text{O}} = \frac{(1 + 2\alpha)I}{2F} \quad \text{and} \quad S_{\text{O}_2} = -\frac{I}{4F} \quad (30)$$

where α is the net water transport coefficient which describes the total water crossover from the anode to cathode through the membrane under combined influences of water diffusion and electro-osmotic drag. Its value is close to zero as recently measured by Liu et al. [44]. In the present work, for simplicity we assume α equal to zero while a non-zero α can be easily incorporated in the present model. Once the reaction rate is available, the following boundary conditions can be applied [45]:

$$\begin{aligned} \rho \vec{u} \cdot \vec{n} &= -(M^{\text{H}_2\text{O}} S_{\text{H}_2\text{O}} - M^{\text{O}_2} S_{\text{O}_2}) \vec{n} \\ \gamma_c \vec{u} C^{\text{H}_2\text{O}} \cdot \vec{n} - D_g^{k,\text{eff}} \frac{\partial C^{\text{H}_2\text{O}}}{\partial n} + \left(\frac{mf_1^k}{M^k} - \frac{C_g^k}{\rho_g} \right) \vec{j}_1 \cdot \vec{n} &= -S^{\text{H}_2\text{O}} \\ \gamma_c \vec{u} C^{\text{O}_2} \cdot \vec{n} - D_g^{\text{O}_2,\text{eff}} \frac{\partial C^{\text{O}_2}}{\partial n} &= -S^{\text{O}_2} \end{aligned} \quad (31)$$

4. Numerical procedures

The governing equations, Eqs. (1), (2), (15) and (22), along with their appropriate boundary conditions are discretized by the finite volume method and solved by a commercial flow solver, Fluent[®] (version 6.0.12), using the SIMPLE (semi-implicit pressure linked equation) algorithm [46]. The SIMPLE algorithm updates the pressure and velocity fields from the solution of a pressure correction equation, solved by algebraic multi-grid (AMG) method. Following the solution of the flow field, species equations are solved. The source terms and physical properties are implemented in a UDF (user-defined function) and the species transport equations are solved through the software's user-defined scalars. The mesh of a single-channel PEFC employed here for a numerical study is shown in Fig. 8. Geometrical and operating parameters are listed in Table 2. Ten thousand ($20 \times 100 \times 5$) computational cells are used to capture the complex two-phase phenomena in the PEFC channel. In addition,

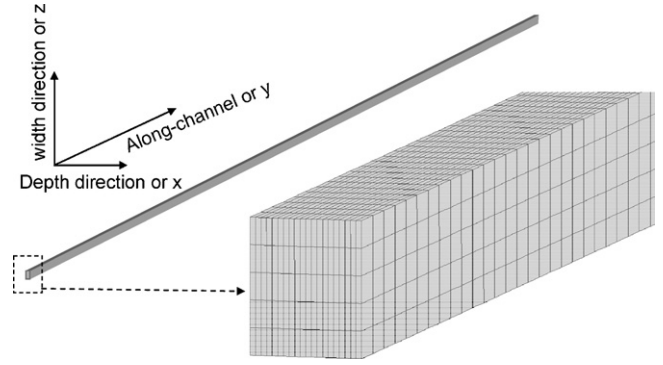


Fig. 8. Geometry and computational mesh of a single straight channel.

Table 2
Geometrical, physical and operating parameters

Quantity	Value
Gas channel depth	0.3 mm
Gas channel width	0.5 mm
Gas channel length	0.1 m
Cathode pressure, P	1.0 atm
Average current density, I_{av}	1.0 A cm ⁻²
Temperature of fuel cell, T	353 K
O ₂ diffusivity in the gas channel at standard condition, D_{o,O_2}	$3.2348 \times 10^{-5} \text{ m}^2 \text{ s}^{-1}$
H ₂ O diffusivity in the gas channel at standard condition, $D_{\text{o},\text{H}_2\text{O}}$	$7.35 \times 10^{-5} \text{ m}^2 \text{ s}^{-1}$
Viscosity of liquid water, μ_l	$3.5 \times 10^{-4} \text{ kg (m s)}^{-1}$
Surface tension, liquid–water–air (80 °C), σ	0.0625 N m ⁻¹
Contact angle of the channel wall, θ_c	80°
Liquid–vapor phase change latent heat, h_{fg}	$2.26 \times 10^6 \text{ J kg}^{-1}$

overall species balance is checked in addition to the equation residuals as important convergence criteria. These species balance checks also ensure physically meaningful results. In all the simulations to be presented in the next section, values of species imbalance are all less than 1% and equation residuals smaller than 10^{-6} .

5. Results and discussion

It is instructive to perform a one-dimensional (along the channel) analysis based on the above-described model. We consider a single-straight channel and the isothermal condition with focus on variations of pressure and liquid saturation along the channel. The cathode side is selected for analysis as shown in Fig. 6(b), while the anode channel problem can be derived similarly.

5.1. Buildup of liquid water

Considering the steady state, integration of Eq. (1) in one-dimension yields:

$$\begin{aligned} A_{xz} \rho u_y &= (A_{xz} \rho u_y)|_{\text{in}} + \int_0^y S_m L_{z,\text{mem}} d\bar{y} \\ &= (A_{xz} \rho u_y)|_{\text{in}} + L_{z,\text{mem}} \frac{\int_0^y I(\bar{y}) d\bar{y}}{2F} M^{\text{H}_2} \end{aligned} \quad (32)$$

where $()|_{\text{in}}$ represents the value of a quantity at the inlet and S_{m} denotes the mass source due to ORR. Note that the net mass source consists of water production minus oxygen consumption. Assuming the capillary effect and diffusive transport along the channel direction are negligible as compared to the convection, integration of Eq. (15) for species water results in:

$$\begin{aligned} A_{xz}\gamma_c u_y C^{\text{H}_2\text{O}} &= (A_{xz}\gamma_c u_y C^{\text{H}_2\text{O}})|_{\text{in}} + \int_0^y S^{\text{H}_2\text{O}} L_{z,\text{mem}} d\bar{y} \\ &= (A_{xz}\gamma_c u_y C^{\text{H}_2\text{O}})|_{\text{in}} + L_{z,\text{mem}} \frac{\int_0^y I(\bar{y}) d\bar{y}}{2F} \end{aligned} \quad (33)$$

where $S^{\text{H}_2\text{O}}$ denotes the water production rate of ORR. Substituting Eq. (32) into Eq. (33) to cancel the mixture velocity, u_y , on the left-hand side yields:

$$\frac{\gamma_c C^{\text{H}_2\text{O}}}{\rho} = \frac{(A_{xz} u_y C^{\text{H}_2\text{O}})|_{\text{in}} + L_{z,\text{mem}} ((\int_0^y I(\bar{y}) d\bar{y})/2F)}{(A_{xz} \rho u_y)|_{\text{in}} + L_{z,\text{mem}} ((\int_0^y I(\bar{y}) d\bar{y})/2F) M^{\text{H}_2}} \quad (34)$$

Using the inlet condition, Eq. (27), one can further express the above as

$$\lambda_l = \frac{(\xi_c/2)(C^{\text{H}_2\text{O}}/C^{\text{O}_2})|_{\text{in}} + ((\int_0^Y I(\bar{Y}) d\bar{Y})/I_{\text{av}}) - (1/\rho_g) C_{\text{sat}}^{\text{H}_2\text{O}} ((\xi_c/2)(\rho/C^{\text{O}_2})|_{\text{in}} + ((\int_0^Y I(\bar{Y}) d\bar{Y})/I_{\text{av}}) M^{\text{H}_2})}{((1/M^{\text{H}_2\text{O}}) - (1/\rho_g) C_{\text{sat}}^{\text{H}_2\text{O}})((\xi_c/2)(\rho/C^{\text{O}_2})|_{\text{in}} + ((\int_0^{Y_0} I(\bar{Y}) d\bar{Y})/I_{\text{av}}) M^{\text{H}_2})} \quad (41)$$

$$\frac{\gamma_c C^{\text{H}_2\text{O}}}{\rho} = \frac{((\xi_c/2) C^{\text{H}_2\text{O}})|_{\text{in}} + ((\int_0^Y I(\bar{Y}) d\bar{Y})/I_{\text{av}})}{((\xi_c/2) \rho)|_{\text{in}} + ((\int_0^Y I(\bar{Y}) d\bar{Y})/I_{\text{av}}) M^{\text{H}_2}} \quad (35)$$

Here, Y is the dimensionless distance from the inlet (see Fig. 8), namely

$$Y = \frac{y}{L_y} = \frac{y}{A_{\text{mem}}} L_{z,\text{mem}} \quad (36)$$

The average current density, I_{av} , can be calculated by integrating the current density profile, $I(Y)$:

$$I_{\text{av}} = \int_0^1 I(\bar{Y}) d\bar{Y} \quad (37)$$

Note that the left-hand side of Eq. (35) is solely determined by liquid water saturation while the right-hand side is a function of operating parameters, such as ξ_c and the inlet humidity, as well as the axial location, Y . Given the expressions of mixture density, Eq. (3), and advection correction factor, Eq. (16), the left-hand side can be further rearranged as

$$\frac{\gamma_c C^{\text{H}_2\text{O}}}{\rho} = \begin{cases} \frac{C^{\text{H}_2\text{O}}}{\rho_g}, & Y < Y_0 \\ \left(\frac{1}{M^{\text{H}_2\text{O}}} - \frac{1}{\rho_g} C_{\text{sat}}^{\text{H}_2\text{O}} \right) + \lambda_l + \frac{1}{\rho_g} C_{\text{sat}}^{\text{H}_2\text{O}}, & Y_0 < Y \end{cases} \quad (38)$$

where Y_0 is the transition point from the single- to two-phase regions, i.e. when $C^{\text{H}_2\text{O}}|_{Y_0} = C_{\text{sat}}^{\text{H}_2\text{O}}$. That is, Y_0 can be determined by setting $C^{\text{H}_2\text{O}}$ on the left-hand side of Eq. (35) to be $C_{\text{sat}}^{\text{H}_2\text{O}}$:

$$\frac{C_{\text{sat}}^{\text{H}_2\text{O}}}{\rho_g} = \frac{((\xi_c/2) C^{\text{H}_2\text{O}})|_{\text{in}} + ((\int_0^{Y_0} I(\bar{Y}) d\bar{Y})/I_{\text{av}})}{((\xi_c/2) \rho)|_{\text{in}} + ((\int_0^{Y_0} I(\bar{Y}) d\bar{Y})/I_{\text{av}}) M^{\text{H}_2}} \quad (39)$$

In the region of $Y < Y_0$, there is single-phase flow in the channel. Note that ρ and ρ_g represent the mixture density and gaseous density respectively and their relation is expressed in Eq. (3). The water concentration can be calculated through Eq. (35) and (38). Other variables, such as O_2 concentration and mixture velocity, can be readily obtained similarly.

Assuming a constant current density, Y_0 can be explicitly expressed as

$$Y_0 = \frac{\xi_c [(1/C^{\text{O}_2})((C_{\text{sat}}^{\text{H}_2\text{O}}/\rho_g)\rho - C^{\text{H}_2\text{O}})]|_{\text{in}}}{2 [1 - (C_{\text{sat}}^{\text{H}_2\text{O}}/\rho_g) M^{\text{H}_2}]} \quad (40)$$

As $\xi_c \rightarrow \infty$, $Y_0 \rightarrow \infty$ unless $C^{\text{H}_2\text{O}}|_{\text{in}} \geq C_{\text{sat}}^{\text{H}_2\text{O}}$. Wang and Wang [45] concluded that the electrochemical reaction has little effect (<5%) on the cathode gas density and flow velocity under common operation of PEFCs. Therefore, Eq. (39) can be further simplified to calculate Y_0 by neglecting mass injection and gas density variation.

In the region of $Y > Y_0$, liquid water emerges and hence there is two-phase flow in the channel. Substituting Eq. (38) into Eq. (35), one obtains:

The liquid mobility, λ_l , is a function of liquid water saturation, s , as shown in Eq. (8) and Fig. 7. Through rearrangement from Eqs. (8) and (9), one can express liquid water saturation explicitly by the liquid mobility, λ_l , as

$$\frac{s - s_{\text{ir}}}{1 - s_{\text{ir}}} = \frac{1}{((1 - \lambda_l)/\lambda_l)(v_g/v_l)^{1/n_k} + 1} \quad (42)$$

Substituting Eq. (41) into Eq. (42), we can obtain an explicit solution of water saturation as a function of operating conditions and axial location. Note that the effect of residual saturation, S_{ir} , has been accounted for in Eq. (42).

Once liquid saturation, s , becomes available, the mixture density can be calculated through Eq. (3), which can further be substituted into Eq. (32) to calculate the mixture velocity by:

$$u_y = \frac{(\rho u_y)|_{\text{in}} + ((\int_0^Y I(\bar{Y}) d\bar{Y})/2F) M^{\text{H}_2}}{\rho} \quad (43)$$

Considering the condition of a constant current density, Eq. (41) can be simplified as

$$\lambda_l = \frac{(\xi_c/2)(C^{\text{H}_2\text{O}}/C^{\text{O}_2})|_{\text{in}} + Y - (1/\rho_g) C_{\text{sat}}^{\text{H}_2\text{O}} ((\xi_c/2)(\rho/C^{\text{O}_2})|_{\text{in}} + Y M^{\text{H}_2})}{((1/M^{\text{H}_2\text{O}}) - (1/\rho_g) C_{\text{sat}}^{\text{H}_2\text{O}})((\xi_c/2)(\rho/C^{\text{O}_2})|_{\text{in}} + Y M^{\text{H}_2})} \quad (44)$$

When full humidification is applied at the inlet, Eq. (44) can be further simplified to:

$$\lambda_l = \frac{(1 - (1/\rho_g) C_{\text{sat}}^{\text{H}_2\text{O}} M^{\text{H}_2})}{((1/M^{\text{H}_2}) - (1/\rho_g) C_{\text{sat}}^{\text{H}_2\text{O}})((\xi_c/2)(\rho/C^{\text{O}_2})|_{\text{in}} + Y M^{\text{H}_2})} Y \quad (45)$$

In the above equation, $\xi_c \rightarrow \infty$ leads to $\lambda_c \rightarrow 0$ and hence $s \rightarrow s_{\text{ir}}$ as shown in Eq. (42).

For the oxygen equation of Eq. (15), following the similar integration, one can arrive at the following formula:

$$\begin{aligned}
 A_{xz} \gamma_c u_y C^{O_2} &= A_{xz} (\gamma_c u_y C^{O_2})|_{in} + \int_0^y S^{O_2} L_{z,mem} dy \\
 &= A_{xz} (\gamma_c u_y C^{O_2})|_{in} - L_{z,mem} \frac{\int_0^y I(\bar{y}) d\bar{y}}{4F}
 \end{aligned}
 \tag{46}$$

Therefore,

$$C^{O_2} = \frac{(\gamma_c u_y C^{O_2})|_{in} - ((\int_0^y I(\bar{Y}) d\bar{Y})/4F)}{\gamma_c u_y}
 \tag{47}$$

The right-hand side of the above equation can be calculated through the known operating conditions and liquid water saturation, s .

Liquid water saturation, s , is an important parameter characterizing the two-phase flow in fuel cell channels. Fig. 9 plots the liquid water saturation profiles along the channel under a full-humidity operation calculated from Eqs. (42) and (45) with the cell temperature of 80 °C and pressure of 100 kPa. We also set the irreducible residual saturation s_{ir} equal to zero to facilitate explaining the results. The effects of the irreducible residual saturation s_{ir} can be readily obtained through Eq. (42). Since the inlet gas is already fully humidified, liquid water emerges at the channel entrance due to local water production. The saturation level rises drastically at the initial stage followed by a slow increase in the downstream. One reason for this trend is that the mobility of liquid water, λ_1 , is strongly dependent on the liquid

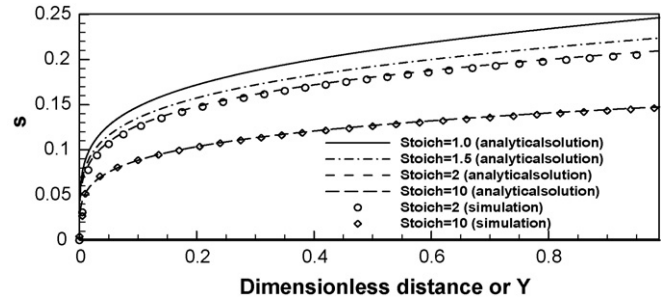


Fig. 9. Liquid water saturation profiles along the channel, predicted from analytical solutions and numerical simulations.

water saturation, as shown in Eqs. (8) and (9), with the value of λ_1 approximately proportional to s^{m_k} at low saturations. Therefore, liquid mobility is very low in low-saturation regions and liquid water builds up quickly as shown in Fig. 9. In addition, it can be seen that the higher the stoichiometric ratio, ξ_c , or the gas flow rate, the lower the saturation level. This can be explained by the fact that higher velocity of the gas is efficient in draining the liquid by overcoming surface interactions. Under common operating conditions of a fuel cell, with $\xi_c = 2.0$, the predicted saturation can reach as high as 20% towards the channel outlet, in good agreement with experimental observations. In addition, 3D simulation results of the cross-section averaged saturation are plotted in the same figure and a good agreement is obtained indicative of validity of the assumptions made in derivation of the analytical solutions.

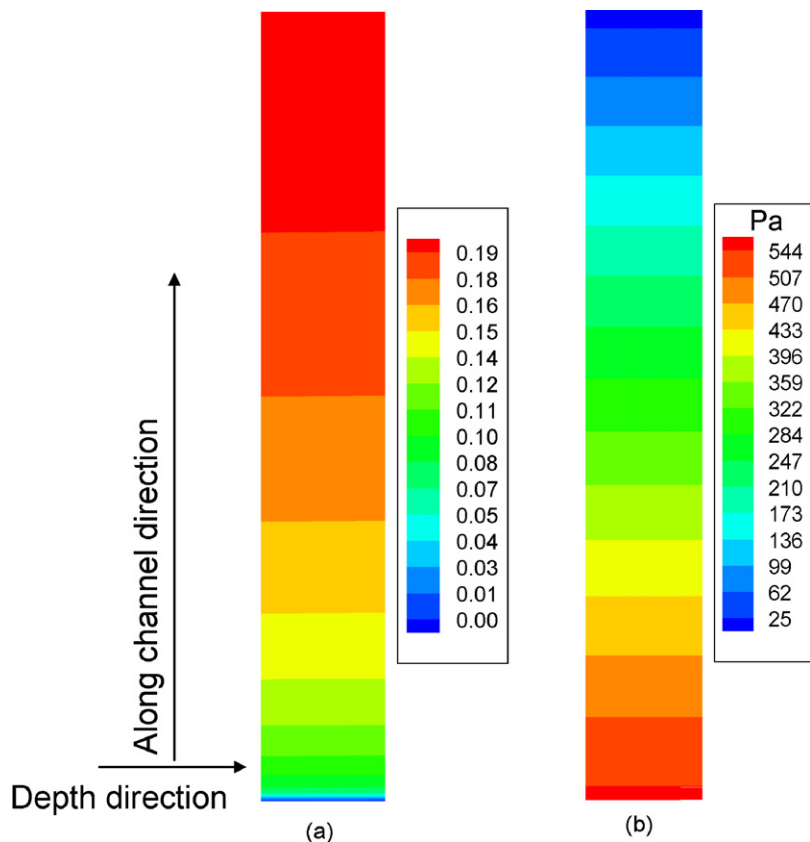


Fig. 10. Simulation results of: (a) liquid water saturation; (b) pressure distribution at the middle cross-section of the channel.

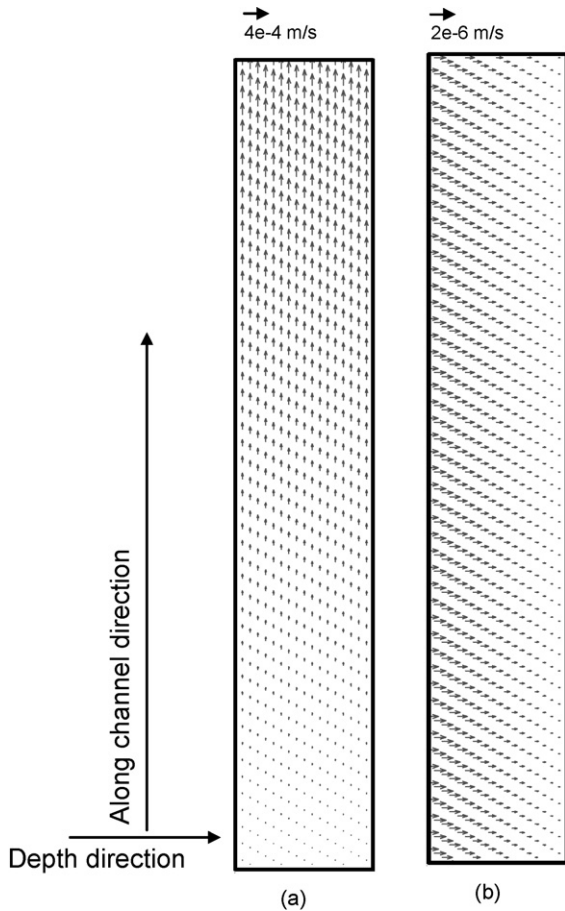


Fig. 11. Simulation results of: (a) liquid phase velocity; (b) component of liquid velocity in the depth direction at the middle cross-section of the channel.

Detailed simulation results are depicted in Figs. 10 and 11, displaying the distributions of liquid water saturation, gas pressure, and liquid velocity in the mid-section of the channel. Fig. 10(a) indicates a small variation of saturation in the depth direction. This is due to the small size of the channel cross-section compared with the channel length. Therefore, a slight liquid water motion exists in the channel depth direction from the GDL–channel interface, where water is injected into the channel, to the opposing sidewall as shown in Fig. 11(b). In addition, Fig. 10(b) indicates that the gas pressure gradient increases along the channel which can be explained by increase of liquid saturation along the channel as shown in Fig. 10(a). Fig. 11(a) shows that the liquid flow along the channel speeds up, due to continual water injection from the GDL–channel interface (the left wall) due to ORR. As the gas phase is already fully saturated at the inlet, the fuel cell channel totally relies on the liquid phase to remove product water. In addition, liquid axial velocity is small along the channel with the magnitude of 10^{-4} m s^{-1} . This velocity magnitude renders a time constant $\sim 1000 \text{ s}$ for water drainage or the reverse process of liquid water accumulation in the channel, given the channel length of 0.1 m. This residence time is consistent with experimental observations on fuel cell transients [47] and much larger than the ones for gas diffusion, membrane hydration [48–50], GDL drying [17,51] and cold start [52,53].

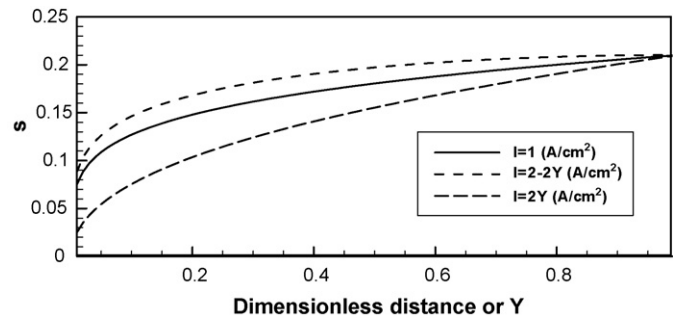


Fig. 12. Analytical results of liquid water saturation profiles under non-uniform current density distribution.

Fig. 12 shows liquid saturation profiles under varying current density distributions as calculated from the analytical solution, Eqs. (41) and (42). As current density is proportional to water production rate, the current density distribution has profound impacts on the local phase distribution as shown in Fig. 12. However, the average current densities are set the same, therefore the same level of liquid water saturation is predicted at the outlet for all the cases despite of different local current density.

While the above results focus on fully saturated gases at the inlet, low-humidity operation is more common in the automotive application of PEFC. Fig. 13 shows simulated profiles of liquid water saturation under different inlet stoichiometric ratios for the inlet gas dew point of 70°C . Because low-humidity gas is fed in, there is no liquid water in the channel entrance region and channel flow is single-phase in nature. As the channel continues receiving water produced from ORR via the GDL, the water concentration in the gas increases till saturation. After that, water addition leads to condensation as the gas is already saturated. This is the transition point from single- to two-phase flow in channels, as clearly shown in Fig. 13. At the initial stage of two-phase flow, the liquid saturation increases gradually due to the fact that a portion of channel flow, near the sidewall opposing to the GDL, is in pure single-phase region which holds water to increase its water content. After the entire channel is in the two-phase regime, the liquid saturation experiences a sharp rise followed by a slow increase towards the channel outlet. In addition, as the air stoichiometry increases, the transition from single- to two-phase flow delays, due to the larger capacity of gas to uptake water vapor before reaching saturation. This con-

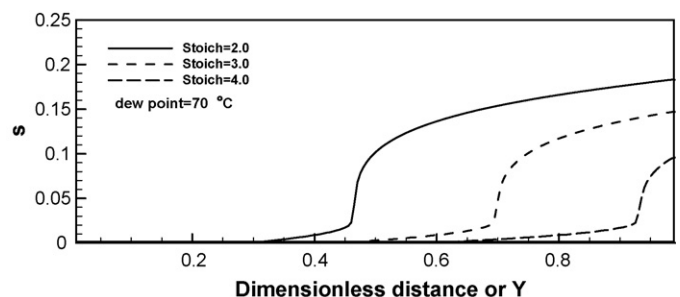


Fig. 13. Simulation results of liquid water saturation distributions under low-humidity inlet conditions.

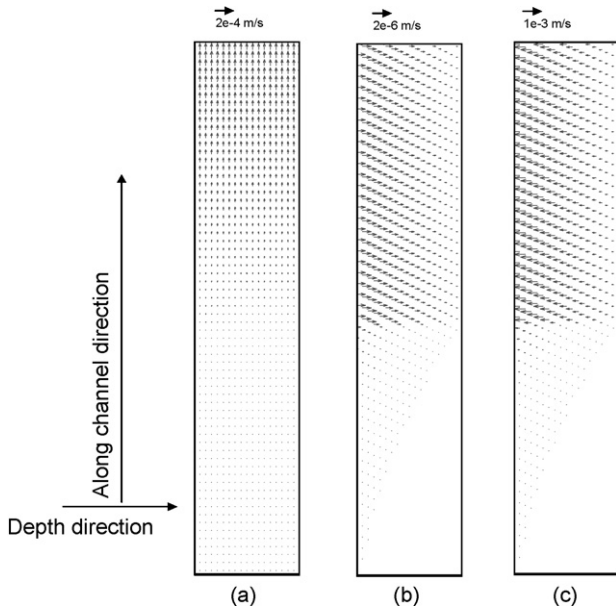


Fig. 14. Simulation results of: (a) liquid velocity; (b) component of liquid velocity in the depth direction; (c) component of gas velocity in the depth direction at the middle of the gas channel.

clusion can also be drawn from the analytical solution for Y_o , Eq. (39).

Fig. 14 shows the simulation results of liquid velocity, velocity components of liquid and gas flow in the depth or x -direction for the inlet stoichiometry of 2 and dew point temperature of 70 °C. It can be seen from Fig. 14(a) that there exists a region where single- and two-phase flows coexist and the liquid flow accelerates after the entire channel is in the two-phase regime. Fig. 14(b) clearly demonstrates that the present M^2 model can resolve differing velocity fields of gas and liquid, indicating that it is a full two-fluid model. The liquid flow in the channel depth direction is away from the GDL surface while the gas flow is towards the GDL, as shown in Fig. 14(c). The magnitude of the transverse gas velocity is small ($\sim 10^{-3} \text{ m s}^{-1}$) compared to the axial gas velocity.

Fig. 15 displays the liquid saturation profiles for different dew point temperatures of inlet gases at the stoichiometry of 2. It can be seen that the higher the gas dew point, the earlier transition into the two-phase flow, as expected.

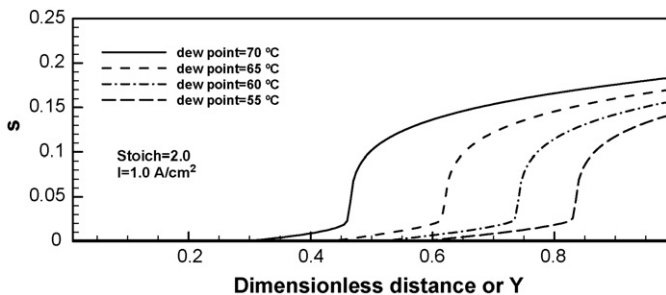


Fig. 15. Analytical solutions of liquid water saturation profiles under low-humidity inlet conditions.

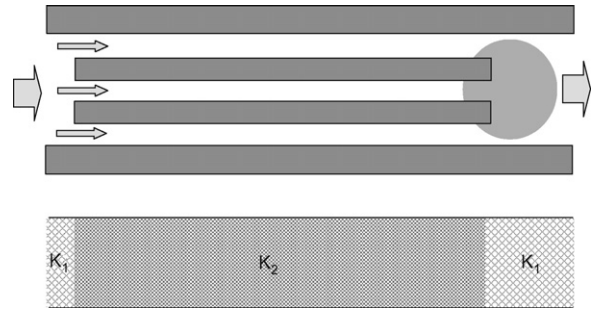


Fig. 16. Schematic of branch-merge flow field and the corresponding porous channel model ($K_1 > K_2$). The cycle shadow represents the liquid water trapping at the heterogeneity.

5.2. Two-phase flow in heterogeneous channels

The foregoing results and discussion have been focused on channels of uniform cross-section and with constant surface wettability, while many PEFC designs have non-uniform channels which feature either geometrical heterogeneity or surface wettability variation along the flow, or both. The two types of heterogeneity are considered together and regarded generally as a spatial variation in channel permeability (or hydraulic conductance) and surface contact angle. For example, a branch-merge channel can be treated as a porous medium with differing permeability or hydraulic conductance, as shown in Fig. 16. This branch-merge flowfield is a popular design in fuel cells due to its ability to mix and re-distribute reactants in channels thereby alleviating a tendency of flow maldistribution. However, the channel design may also lead to water trapping at the transition point as shown in Fig. 16. In addition, a branch of parallel channels in a fuel cell usually share the same inlet or outlet, also called manifold as shown in Figs. 3 and 4, which resembles either the merge or branched pattern.

For liquid water transport through a homogeneous porous channel, the capillary action can be written, through substituting Eq. (19) into the second term on the right-hand side of Eq. (15), as

$$\nabla \cdot \left[\left(\frac{mf_1^k}{M^k} - \frac{C_g^k}{\rho_g} \right) \vec{j}_l \right] = \nabla \cdot \left[\left(\frac{mf_1^k}{M^k} - \frac{C_g^k}{\rho_g} \right) \frac{\lambda_l \lambda_g}{\nu} K \nabla P_c \right] \quad (48)$$

The above term can be treated as a diffusion term with the following form:

$$\nabla \cdot \left[\left(\frac{mf_1^k}{M^k} - \frac{C_g^k}{\rho_g} \right) \vec{j}_l \right] = \nabla \cdot \left[\left(\frac{mf_1^k}{M^k} - \frac{C_g^k}{\rho_g} \right) \frac{\lambda_l \lambda_g}{\nu} K \frac{dP_c}{ds} \nabla s \right] \quad (49)$$

Thus, the capillary force drives water from a higher saturation to a lower saturation region in a homogenous porous medium. However, in a heterogeneous porous medium, Eq. (48) must be

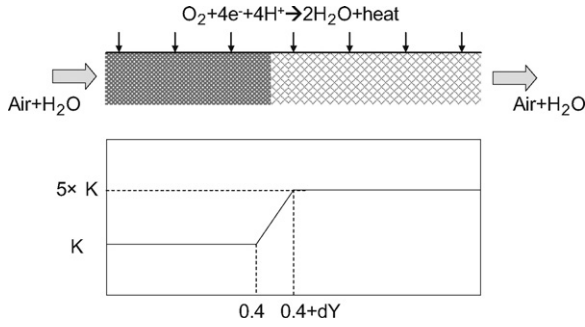


Fig. 17. Schematic of permeability heterogeneity in fuel cell channels.

rewritten in the following general form:

$$\begin{aligned} \nabla \cdot \left[\left(\frac{mf_1^k}{M^k} - \frac{C_g^k}{\rho_g} \right) \frac{\lambda_1 \lambda_g}{\nu} K \nabla P_c(\sigma, \theta_c, \varepsilon, K, s) \right] \\ = \nabla \cdot \left[\left(\frac{mf_1^k}{M^k} - \frac{C_g^k}{\rho_g} \right) \frac{\lambda_1 \lambda_g}{\nu} K \left(\frac{\partial P_c}{\partial \sigma} \nabla \sigma + \frac{\partial P_c}{\partial \theta_c} \nabla \theta_c \right. \right. \\ \left. \left. + \frac{\partial P_c}{\partial \varepsilon} \nabla \varepsilon + \frac{\partial P_c}{\partial K} \nabla K + \frac{\partial P_c}{\partial s} \nabla s \right) \right] \end{aligned} \quad (50)$$

It can be seen that spatial variations in surface tension σ , contact angle θ_c , porosity ε and permeability K add extra terms into the capillary action in addition to the capillary diffusion under saturation gradient. For simplicity, here we only consider the heterogeneity in the permeability (or hydraulic conductance), K , while keeping other properties constant. Then the additional term due to geometrical heterogeneity can be expressed as

$$\begin{aligned} \nabla \cdot \left[\left(\frac{mf_1^k}{M^k} - \frac{C_g^k}{\rho_g} \right) \frac{\lambda_1 \lambda_g}{\nu} K \left(\frac{\partial P_c}{\partial K} \nabla K \right) \right] \\ = \nabla \cdot \left[\left(\frac{mf_1^k}{M^k} - \frac{C_g^k}{\rho_g} \right) \frac{\lambda_1 \lambda_g \sigma \cos(\theta_c) \varepsilon^{1/2}}{\nu} J(s) K \nabla (K^{-1/2}) \right] \end{aligned} \quad (51)$$

Further assuming a linear profile of K along the channel, as shown in Fig. 17

$$K = k_1 y + k_2 \quad (52)$$

One can reach

$$K \nabla (K^{-1/2}) = K \begin{pmatrix} 0 \\ -\frac{1}{2} k_1 K^{-3/2} \\ 0 \end{pmatrix} = -\frac{1}{2} k_1 \begin{pmatrix} 0 \\ K^{-1/2} \\ 0 \end{pmatrix} \quad (53)$$

Fig. 18 shows the liquid water saturation profile along a heterogeneous channel schematically shown in Fig. 17. It can be seen that the saturation profile remains almost unchanged in the uniform sections of the channel while a spike is predicted in the heterogeneous region. This result indicates that the influence of local heterogeneity affects only the local phase distribution.

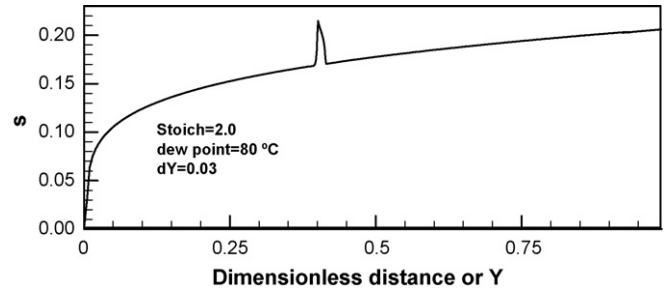


Fig. 18. Simulation result of the liquid water saturation around the heterogeneity shown in Fig. 17.

This localized phenomenon can be readily explained by Eq. (50) where the extra term acts like an additional capillary force to hold up water. On the global scale, since the extra terms in Eq. (50) are mathematically in conservative form, there is no extra water added besides water production by ORR. Finally, it is noteworthy that if reaching a high-liquid saturation, the localized spike may cause channel clogging by liquid water and flow shutdown in a multiple, parallel channel configuration.

It should be noted that while Eq. (50) is derived for isotropic porous media, a similar analysis could be performed for anisotropic media. More discussion on two-phase flows in heterogeneous porous media can be found in the field of petroleum and geological systems [26,32].

5.3. Two-phase pressure drop

As the presence of liquid water hampers gas flow in fuel cell channels, the gas pressure gradient in two-phase flow is greater than that in single-phase. The increased pressure drop due to liquid water accumulation is a key cause for flow maldistribution, as schematically shown in Fig. 19. Liquid water in the lower channel incurs additional pressure drop which forces the gas flowrate to be reduced in the lower channel and increased in the upper channel in order to maintain the same pressure drop between the inlet and outlet manifolds. Such a two-phase flow maldistribution dramatically reduces PEM fuel cell performance as well as durability.

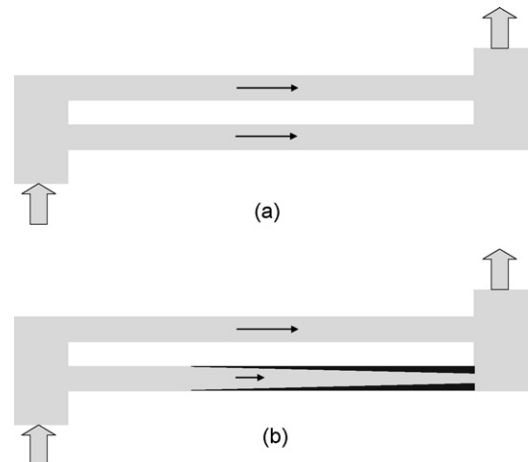


Fig. 19. Schematic of flow in multiple channels: (a) uniform distribution; (b) maldistribution. The black shadowed regions in (b) denote the liquid phase.

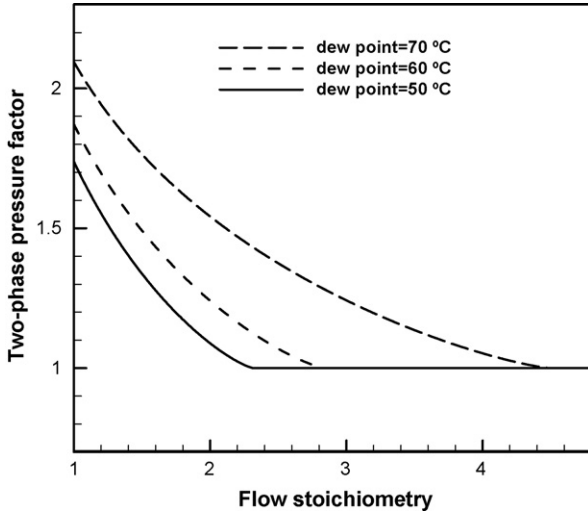


Fig. 20. Two-phase pressure factor vs. the stoichiometric flow ratio under different inlet humidities for a single channel ($n_k = 4$).

The gas pressure gradient is linked to the gas velocity via the Darcy’s law, namely

$$u_g = -\frac{K(1-s)^{n_k}}{\mu_g L_y} \frac{dp_g}{dY} \quad (54)$$

In view of the nitrogen content of ~79% in air, we can safely assume that the gas velocity remains nearly constant along the channel, equal to the inlet value, $u_g \approx u_{in,c}$. Indeed, Wang and Wang [45] numerically showed that variation of the gas phase velocity is small (<5%) in common PEFC operation. Thus, Eq. (54) can be rearranged to:

$$\frac{dp_g}{dY} = -\frac{I_{av} A_{mem}}{4F} \frac{1}{C^{O_2} A_{xz}} \frac{\mu_g L_y}{K} \frac{\xi_c}{(1-s)^{n_k}} \quad (55)$$

If a dimensionless pressure is defined as

$$|\Delta P| = \frac{|\Delta p_g|}{(I_{av} A_{mem}/4F)(1/C^{O_2} A_{xz})(\mu_g L_y/K)} \quad (56)$$

One obtains that

$$|\Delta P| = \xi_c \int_0^1 \frac{1}{[1-s(Y, \xi_c, RH_{in})]^{n_k}} dY = |\Delta P(\xi_c)| \quad (57)$$

Eq. (57) shows that the dimensionless pressure drop is only a function of the air stoichiometry ξ_c and inlet humidity, RH. In the single-phase regime, Eq. (57) is reduced to:

$$|\Delta P^{1\phi}| = \xi_c \quad (58)$$

Thus, a two-phase pressure factor, Φ , can be defined as

$$\Phi = \frac{|\Delta P|}{|\Delta P^{1\phi}|} = \int_0^1 \frac{1}{[1-s(Y, \xi_c, RH_{in})]^{n_k}} dY \quad (59)$$

Eq. (59) indicates that the two-phase pressure factor depends only on the air stoichiometry and inlet RH. Fig. 20 shows the analytical result of the two-phase pressure factor as a function of stoichiometric ratio for different inlet dew points or RHs. It can be seen that at low-stoichiometric ratios or low-channel flow rates, the two-phase pressure factor is greater than unity due to

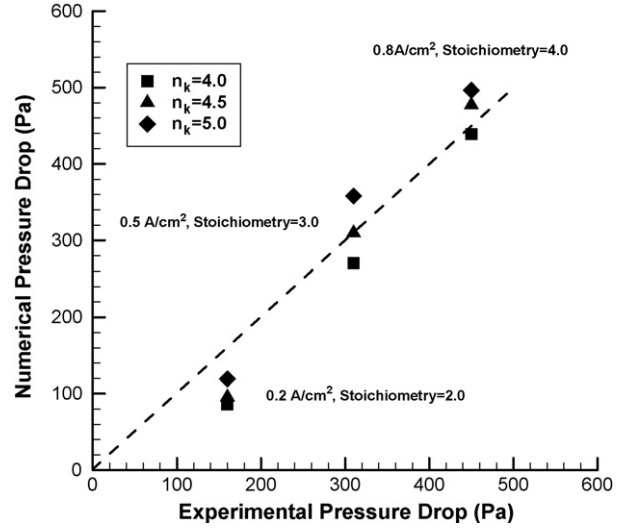


Fig. 21. Experimental validation of the channel two-phase model.

liquid water presence. As the flow rate increases, the occurrence of two-phase flow shifts more towards the downstream and hence the two-phase pressure factor is lower and approaches unity. Also, Eq. (59) clearly indicates that the exponent, n_k , is a key factor determining the two-phase pressure factor. Therefore, one can measure the two-phase pressure drop across the fuel cell channels in order to calibrate n_k , as to be explained briefly in the next sub-section.

5.4. Experimental validation

To experimentally validate the above-described channel two-phase model and to better understand the applicable range of n_k specifically for fuel cell channels, a seven-parallel-channel fuel cell of 0.1 m long was designed and pressure drop measurements were carried out. While experimental details have been documented by Hussaini and Wang [55] and thus are not repeated here, the experimental data of two-phase pressure drop, selected over a range of air stoichiometry and current density to be representative, are plotted in Fig. 21, after excluding any influence from inlet and outlet manifolds. These average data for straight channels can then be compared with the present model prediction for a single channel, as shown in Fig. 21. It is seen that there is slight under-prediction using $n_k = 4$. However, the experimental-model agreement is good for both $n_k = 4.5$ and 5.0. It can thus be concluded that the present channel two-phase model is reasonably accurate and the exponent in the liquid permeability likely lies between 4.5 and 5.0.

6. Conclusions

In this work, we have developed a two-phase model for channel flow in a PEM fuel cell, based on the M^2 formalism. Theoretical analyses were performed to calculate the liquid water saturation, onset location of two-phase flow, and species concentrations along the channel. Dependence of these physical profiles vital to cell performance on key operating parameters such as air stoichiometry and relative humidity is explored. An analytical

solution was developed to express the liquid water saturation as a function of the stoichiometric ratio, relative humidity, and axial location. The model was further implemented for three-dimensional numerical simulations of two-phase flow in a single channel. The results reveal that liquid water builds up quickly at the entrance region followed by a slow increase downstream, under full-humidification inlet conditions. The predicted liquid saturation reaches as high as 20%. Subsequently, two-phase flow in heterogeneous channels were theoretically analyzed and numerically simulated. Water trapping around the geometrical heterogeneity was found. In addition, a two-phase pressure factor was defined which could help establish a fundamental understanding of two-phase flow maldistribution in fuel cell channels. Finally, preliminary validation of the present channel two-phase model against experimental pressure drop data was carried out, with good agreement. Future work is to validate the present model against experimental liquid water saturation profiles once they are available, as well as to integrate the channel two-phase model into a full cell model.

Appendix A. Nomenclature

A	area (m^2)
C^k	molar concentration of species k (mol m^{-3})
D	mass diffusivity of species ($\text{m}^2 \text{s}^{-1}$)
F	Faraday's constant (96,487 C/equivalent)
I	current density (A cm^{-2})
k	thermal conductivity (W (m K)^{-1})
k_r	relative permeability
K	permeability (m^2)
L	length (m)
mf_1^k	mass fraction of species k in liquid phase
M	molecular weight (kg mol^{-1})
n	the direction normal to the surface
P	pressure (Pa)
R	gas constant ($8.134 \text{ J (mol K)}^{-1}$)
s	stoichiometry coefficient in electrochemical reaction or liquid saturation
S	source term in transport equations
t	time (s)
T	temperature (K)
\vec{u}	velocity vector (m s^{-1})
X	mole fraction

Greek letters

α	net water transport coefficient per proton
ε	porosity
κ	ionic conductivity (S m^{-1})
λ_k	mobility of phase k
ν	kinematic viscosity ($\text{m}^2 \text{s}^{-1}$)
ξ	stoichiometric flow ratio
ρ	density (kg m^{-3})
σ	surface tension (N m^{-1})
τ	tortuosity factor
Φ	two-phase pressure factor

Superscripts and subscripts

a	anode
av	average
c	cathode
eff	effective value
g	gas phase
in	inlet
k	species
l	liquid phase
mem	membrane
o	standard condition, 273.15 K and 101.3 kPa (1 atm)
sat	saturate value

References

- [1] M.L. Perry, T.F. Fuller, J. Electrochem. Soc. 149 (2002) S59–S67.
- [2] C.Y. Wang, Chem. Rev. 104 (2004) 4727–4765.
- [3] P. Costamagna, S. Srinivasan, J. Power Sources 102 (2001) 242–252.
- [4] P. Costamagna, S. Srinivasan, J. Power Sources 102 (2001) 253–269.
- [5] Z.H. Wang, C.Y. Wang, K.S. Chen, J. Power Sources 94 (2001) 40–50.
- [6] J.-H. Nam, M. Kaviany, Int. J. Heat Mass Transfer 46 (2003) 4595–4611.
- [7] U. Pasaogullari, C.Y. Wang, J. Electrochem. Soc. 151 (2004) A399–A406.
- [8] X.G. Yang, F.Y. Zhang, A. Lubawy, C.Y. Wang, Electrochem. Solid-State Lett. 7 (2004) A408–A411.
- [9] F.Y. Zhang, X.G. Yang, C.Y. Wang, J. Electrochem. Soc. 153 (2006) A225–A232.
- [10] D. Natarajan, T.V. Nguyen, J. Electrochem. Soc. 48 (12) (2001) 1324–1335.
- [11] S. Mazumder, J.V. Cole, J. Electrochem. Soc. 150 (2003) A1510–A1517.
- [12] A.Z. Weber, J. Newman, J. Electrochem. Soc. 152 (4) (2005) A679–A688.
- [13] U. Pasaogullari, C.Y. Wang, J. Electrochem. Soc. 152 (2005) A380–A390.
- [14] E. Birgersson, M. Noponen, M. Vynnycky, J. Electrochem. Soc. 152 (2005) A1021–A1034.
- [15] H. Meng, C.Y. Wang, J. Electrochem. Soc. 152 (2005) A1733–A1741.
- [16] Y. Wang, C.Y. Wang, J. Electrochem. Soc. 153 (6) (2006) A1193–A1200.
- [17] Y. Wang, C.Y. Wang, J. Electrochem. Soc. 154 (2007) B636–B643.
- [18] K. Promislow, J. Stockie, B. Wetton, Proc. R. Soc. A 462 (2006) 789–816.
- [19] T.V. Nguyen, W. He, in: W. Vielstich, H. Gasteiger, A. Lamm (Eds.), Handbook of Fuel Cells: Fundamentals, Technology and Applications, vol. 3, John Wiley & Sons, Ltd., 2003 (Chap. 28).
- [20] T.V. Nguyen, J. Electrochem. Soc. 143 (5) (1996) L103–L105.
- [21] D.P. Wilkinson, O. Vanderleeden, in: W. Vielstich, H. Gasteiger, A. Lamm (Eds.), Handbook of Fuel Cells: Fundamentals, Technology and Applications, vol. 3, John Wiley & Sons, Ltd., 2003 (Chap. 27).
- [22] X. Li, I. Sabir, Int. J. Hydrogen Energy 30 (4) (2005) 359–371.
- [23] Y. Wang, C.Y. Wang, J. Power Sources 147 (2005) 148–161.
- [24] Y. Wang, C.Y. Wang, J. Power Sources 153 (2006) 130–135.
- [25] Y. Wang, C.Y. Wang, K.S. Chen, Electrochim. Acta. 52 (2007) 3965–3975.
- [26] A.S. Stubos, C. Satik, Y.C. Yortsos, Int. J. Heat Mass Transfer 36 (1993) 967–976.
- [27] C.Y. Wang, M. Groll, S. Rosler, C.J. Tu, Heat Recov. Syst. CHP 14 (4) (1994) 377–389.
- [28] K.-K. Tio, C.Y. Liu, K.C. Toh, Heat Mass Transfer 36 (2000) 21–28.
- [29] U. Imke, Chem. Eng. J. 101 (2004) 295–302.
- [30] T. Henning, J.J. Brandner, K. Schubert, Microfluid Nanofluid 1 (2005) 128–136.
- [31] D. Sugumar, K.K. Tio, J. Heat Transfer 128 (2) (2006) 198–202.
- [32] M. Chaouche, N. Rakotomalala, D. Salin, Y.C. Yortsos, Europhys. Lett. 21 (1993) 19–24.
- [33] D. Or, M. Tuller, Adv. Water Resour. 26 (2003) 883–898.
- [34] W. Li, R.D. Vigil, I.A. Beresnev, P. Iassonov, R. Ewing, J. Colloid Interf. Sci. 289 (2005) 193–199.
- [35] J.D. Chen, J. Colloid Int. Sci. 109 (2) (1986) 341–349.
- [36] H. Wong, S. Morris, C.J. Radke, J. Colloid Interf. Sci. 148 (1992) 317–336.
- [37] C.Y. Wang, P. Cheng, Int. J. Heat Mass Transfer 39 (1996) 3607–3618.
- [38] T. Benning, N. Djilali, J. Electrochem. Soc. 150 (2003) A1589–A1598.

- [39] A.T. Corey, *Producers Monthly* 19 (1) (1954) 38–41.
- [40] A.E. Saez, R.G. Carbonell, *AIChE J.* 31 (1985) 52–62.
- [41] R.B. Bird, W.E. Stewart, E.N. Lightfoot, *Transport Phenomena*, John Wiley & Sons, New York, 1960.
- [42] M. Mathias, J. Roth, J. Fleming, W. Lehnert, in: W. Vielstich, H. Gasteiger, A. Lamm (Eds.), *Handbook of Fuel Cells: Fundamentals, Technology and Applications*, vol. 3, John Wiley & Sons, Ltd., 2003.
- [43] T.E. Springer, T.A. Zawodinski, S. Gottesfeld, *J. Electrochem. Soc.* 138 (1991) 2334–2341.
- [44] F.Q. Liu, G.Q. Lu, C.Y. Wang, *J. Membr. Sci.* 287 (2007) 126–131.
- [45] Y. Wang, C.Y. Wang, *J. Electrochem. Soc.* 152 (2005) A445–A453.
- [46] S.V. Patankar, *Numerical Heat Transfer and Fluid Flow*, Hemisphere Publishing Corp., New York, 1980.
- [47] J. Benziger, E. Chia, E. Karnas, J. Moxley, C. Teuscher, I. Kevrekidis, *AIChE J.* 50 (2004) 1889–1900.
- [48] Y. Wang, C.Y. Wang, *Electrochim. Acta* 50 (2005) 1307–1315.
- [49] Y. Wang, C.Y. Wang, *Electrochim. Acta* 51 (2006) 3924–3933.
- [50] H. Meng, *J. Power Sources* 171 (2007) 738–746.
- [51] Y. Wang, *Analysis of transient phenomena in polymer electrolyte fuel cells*, PhD thesis, The Pennsylvania State University, 2006.
- [52] L. Mao, C.Y. Wang, *J. Electrochem. Soc.* 154 (2007) B139–B146.
- [53] Y. Wang, *J. Electrochem. Soc.* 154 (2007) B1041–B1048.
- [54] X.G. Yang, F.Y. Zhang, C.Y. Wang, private communications, 2005.
- [55] I.S. Hussaini, C.Y. Wang, *Visualization and quantification of cathode channel flooding in PEM fuel cells*, Penn State University Electrochemical Engine Center (ECEC), Report No. 2007-07 (2007).